Laser-induced Coulomb-explosion imaging of the CS₂ dimer: The effect of non-Coulombic interactions

Constant A. Schouder,[1] Adam S. Chatterley,[1] Lars Bojer Madsen ●,[2] Frank Jensen ●,[1] and Henrik Stapelfeldt ●[1]

[1]*Department of Chemistry, Aarhus University, Langelandsgade 140, DK-8000 Aarhus C, Denmark*

[2]*Department of Physics and Astronomy, Aarhus University, Ny Munkegade 120, DK-8000 Aarhus C, Denmark*

Carbon disulfide dimers $(CS_2)_2$ are doubly ionized by an intense 40-fs laser pulse leading to fragmentation into a pair of CS_2^+ cations. Unlike previous studies on atomic dimers, their kinetic energy, gained by mutual electrostatic repulsion, deviates strongly from the value determined by applying the Coulomb interaction approximation to the $(CS_2)_2^{2+}$ ion. An *ab initio* calculation shows that inclusion of non-Coulombic interactions in $(CS_2)_2^{2+}$ is crucial to account for the observed kinetic energy. These interactions result in 16 $(CS_2)_2^{2+}$ electronic microstates, which obstructs accurate determination of intermolecular bond distances in $(CS_2)_2$ from the fragments' kinetic energy. The situation will be similar for most other weakly bonded atomic and molecular complexes.

I. INTRODUCTION

Molecular Coulomb explosion is a process that occurs when, for instance, an intense fs laser pulse multiply ionizes a molecule and the resulting multiply-charged molecular cation breaks apart into cationic fragments due to their internal electrostatic repulsion. The structure and spatial orientation of the molecule at the instant the electrons are removed, define the emission direction and kinetic energy of the fragments. Coulomb explosion imaging (CEI) is the technique that aims at determining molecular structure by recording these experimental observables [1,2].

One focus of CEI is the determination of bond distances and internuclear wave functions [3–5]. This relies on approximating the fragments as point charges and thus their potential energy by the Coulomb interaction. For a two-body system, the potential energy (atomic units are used throughout) is $V(R) = \frac{q_1 q_2}{R}$, where q_1 and q_2 are the charges of the fragments and R their separation. As the fragments move apart, $V(R)$ is converted into kinetic energy and therefore the initial potential energy can be determined by measuring the final kinetic energy E_{kin} of the fragments. Hereby, $R_{initial}$ is obtained as $\frac{q_1 q_2}{E_{kin}}$, which will also equal the corresponding bond distance in the parent molecule provided the electron removal is sufficiently fast.

A key question is when the point charge approximation (PCA) of the fragments is sufficiently good that CEI can provide accurate determinations of bond distances and wave functions. This has been shown to be the case for Coulomb explosion of H_2^+ into two H^+ [3,4,6,7], and for Coulomb explosion of a dissociating diatomic molecule, like I_2, with R so large that the molecule essentially consisted of two separated atoms [5,8,9]. In contrast, for most covalently bonded molecules in their equilibrium geometry, Coulomb explosion does not capture the bond distances well [10,11] because the potential curves of the multiply charged molecular cations deviate significantly from Coulomb potentials due to residual molecular bonding [12–14].

Over the past decade, fs laser-induced CEI has also been applied to van der Waals dimers or larger oligomers. In particular, homodimers, trimers, and tetramers of noble gas atoms, and heterodimers composed of a noble gas atom and a diatomic molecule were explored [15–21]. Using the PCA for the recoiling fragment ions, equilibrium structures, including accurate interatomic distances, were reported and in some cases, even the interatomic wave function. The validity of the PCA has, however, never been investigated for such weakly-bonded complexes.

Here, we address this issue by exploring if fs laser-induced CEI can be used to determine the equilibrium separation between the two monomers in a van der Waals dimer of molecules, and possibly the intermolecular wave function. As a test case, the crossed-shaped CS_2 dimer [Fig. 1(a)] is doubly ionized leading to two CS_2^+ fragments. The CS_2 dimer was chosen both due to its symmetric shape and because intermolecular motion following single ionization [22] is negligible during the laser pulse, due to the rather large mass of the CS_2 monomers and the shallow potential of the $(CS_2)_2^+$ cation, see Sec. A1.

II. EXPERIMENTAL SETUP

The experimental setup has been described before [23], so only a few pertinent details are given. A gas of 80 bar He is passed over a sample of liquid CS_2 at room temperature and then expanded through an Even Lavie valve into the source chamber of a molecular beam instrument. The molecular beam formed is skimmed and sent into a velocity map imaging (VMI) spectrometer where it is crossed by a linearly polarized, focused laser beam. The 40-fs long (FWHM) pulses in the laser beam (400 nm, 1×10^{14} W/cm²) ionizes CS_2 monomers and dimers, the main constituents of
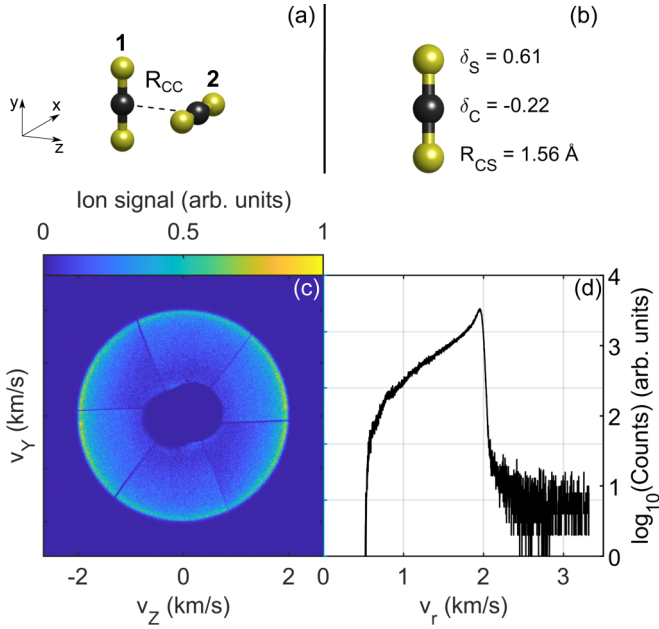
FIG. 1. (a) Sketch of the CS_2 dimer structure [26]. (b) Partial charges in the CS_2^+ ion in units of $|e|$. (c) Coincidence filtered (see text) 2D velocity image of CS_2^+ ions. The probe laser beam is polarized along the Y axis. (d) Velocity distribution of the CS_2^+ ions in the detector plane, obtained from the image in (c).

FIG. 2. (a) E_{kin} distributions. Purple curve: experimental result. Dashed curves are the simulated results with the following potentials. Yellow: point charge; red: partial charges; blue: quantum chemistry (QC); black: QC with the spin-orbit interaction and including all microstates (see text). (b) R_{CC} distributions. Full curves are the experimental data using the point charge (yellow); partial charge (red); QC (blue); QC including spin orbit, averaged over all microstates (black) potential models of the dimer dication. The dashed black curve is $|\Psi_{v=0}(R_{CC})|^2$ for the potential curve of $(CS_2)_2$, shown in Fig. 3(a).

the molecular beam. The VMI spectrometer accelerates the cations formed onto a MCP detector backed by a phosphor screen, and thereby the 2D projection of the velocity vector for each CS_2^+ ion can be recorded by a CCD camera. The MCP detector is gated such that only the $^{12}C^{32}S_2^+$ isotopologue is detected. The velocity projection is denoted by the coordinates (v_r, θ), where v_r is the velocity in the detector plane of the ion hit (proportional to its radius) and θ its angle with the laser polarization, kept in the detector plane. The term, frame, describes the ion hits resulting from a single laser shot whereas an, image, is the sum of a number of frames. The repetition rate of the measurements is 200 Hz.

III. RESULTS

The basic experimental data of this work are a 2D velocity image of CS_2^+ ions resulting from the sum of 3.85×10^5 frames and containing $\sim 1.5 \times 10^7$ ion hits. A metal disk was installed in front of the detector to remove the large contribution of CS_2^+ ions originating from ionization of CS_2 monomers. This explains the central zero-signal area and the radial stripes, coming from the disk supports, in the ion image shown in Fig. 1(c). This image is obtained from applying a coincidence filter to the original image [24]. The filter discards an ion hit (v_{r1}, θ_1) unless there is a partner ion hit (v_{r2}, θ_2) in the same frame such that: $179.1° < |\theta_2 - \theta_1| < 180.9°$ and $|v_{r2} - v_{r1}| < 48 m/s$. We identify the ions in the ring with a radius of ~ 2 km/s as originating from a $(CS_2)_2^{2+} \rightarrow CS_2^+ + CS_2^+$ Coulomb explosion channel because the filter retains only CS_2^+ ions from a symmetric two-body breakup. The angular anisotropy of the ions in the ring is, we believe, due to an alignment-dependent double ionization probability [25]
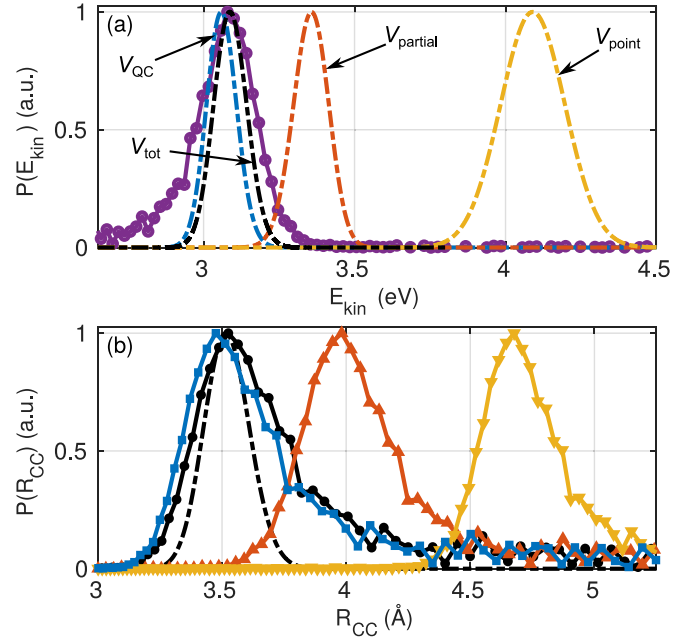
of the dimer.[1] The ring manifests itself as a single peak at $v_r = 2$ km/s in the radial distribution, Fig. 1(d), of the image in Fig. 1(c). We now analyze this peak to find out if it contains information about the intermolecular distance of the dimer and possibly the intermolecular wave function.

The first step is to determine the kinetic energy distribution, $P(E_{kin})$ of the CS_2^+ ions. This involves Abel inverting the filtered image in Fig. 1(c), and from the inverted image, extracting the radial velocity distribution, and then converting to kinetic energy by application of a calibration factor and a standard Jacobian transform. To determine this factor accurately, the VMI spectrometer was calibrated just prior to the measurements, see Sec. A. From this calibration, we estimate an uncertainty in kinetic energy of $\pm 2\%$, limited primarily by the resolution of the camera. The purple curve in Fig. 2(a) shows $P(E_{kin})$ of the two CS_2^+ ions. It peaks at ~ 3.1 eV and has a FWHM of ~ 320 meV with a slight asymmetry towards lower values.

To understand the experimental data, we first calculated $P(E_{kin})$ of the CS_2^+ ions applying the PCA, i.e., assuming that the potential curve for $(CS_2)_2^{2+}$ is given by $V_{point} = 1/R_{CC}$ [Fig. 3(a)], where R_{CC} is the intermolecular distance, see

---

[1]The ionization rate is minimized when the least polarizable axis of $(CS_2)_2$, the C-C axis [38], is parallel to the probe pulse polarization (the Y axis). This explains why the angular distribution of the CS_2^+ ions has a minimum along the Y axis.
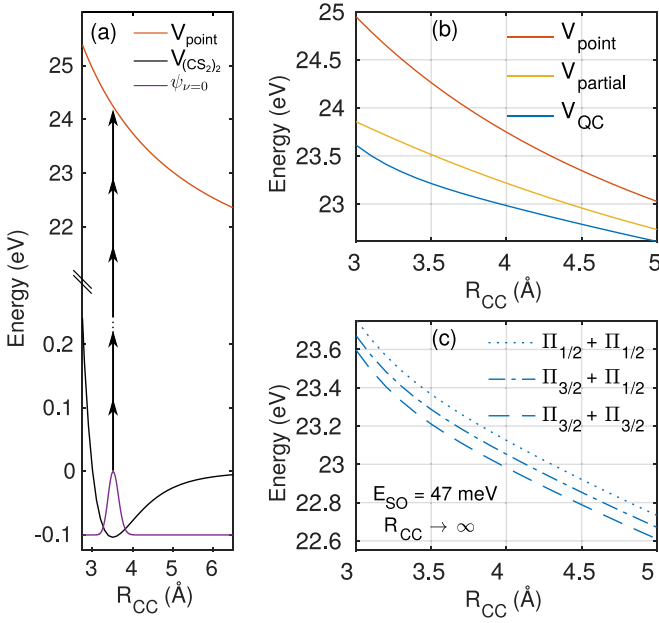
FIG. 3. (a) Energy diagram of the CS_2 dimer showing the wave function of the vibrational ground state and its projection, by multi-photon absorption from the probe pulse, onto the repulsive Coulomb potential corresponding to a point charge model of $(CS_2)_2^{2+}$. (b) The three potential curves, V_{point}, $V_{partial}$, and V_{QC} used to model $(CS_2)_2^{2+}$, in the region around the equilibrium distance of $(CS_2)_2$. (c) The splitting of V_{QC} into three groups of potential curves due to different hole configurations and spin-orbit interaction. The energy splitting, E_{SO}, between each curve when $R_{CC} \to \infty$ is shown in the legend/on the lower left corner.

Fig. 1(a). This approximation is the one used in previous works on Ar_2, Ne_2, ArO_2, ArN_2, and XeO_2 [17–21]. Under our experimental conditions, the CS_2 dimers are in the inter-molecular vibrational ground state [24]. Consequently, for the initial distribution of R_{CC}, needed to calculate E_{kin} of the CS_2^+ ions, we used $|\Psi_{v=0}(R_{CC})|^2$, where $\Psi_{v=0}(R_{CC})$ is the wave function of the lowest vibrational state in the intermolecular potential along the R_{CC} coordinate, see Fig. 3(a). The inter-molecular potential for $(CS_2)_2$ was calculated at the CCSD(T) frozen-core level with the aug-cc-pVTZ and aug-cc-pVQZ basis sets. The results were corrected for basis set superposition errors by the counter poise method [27] and extrapolated to the complete basis set limit by an L^{-3} formula [28]. The basis set convergence indicates that the shape of the potential energy curves is converged to within 10 cm^{-1} for $R_{CC} \geqslant 3.0$ Å.

To convert the calculated intermolecular distribution, $P(R_{CC})$ to $P(E_{kin})$, we computed the overlap between $\Psi_{v=0}$ and the continuum wave functions ϕ_{cont}, pertaining to the potential V_{dicat} of $(CS_2)_2^{2+}$:

$$P(E_{kin}) = \left| \int \phi_{cont}^*(R_{CC}) \Psi_{v=0}(R_{CC}) dR_{CC} \right|^2. \quad (1)$$

Here ϕ_{cont} were calculated with the Numerov method in the energy range of 2–6 eV. The yellow curve in Fig. 2(a) shows $P(E_{kin})$ of the CS_2^+ ions determined by the point charge model, i.e., $V_{dicat} = V_{point}$. The calculated distribution is centered at 4.1 eV, about 1 eV higher than the measured

distribution. The same pronounced disagreement between experimental and simulated results is evident when the measured $P(E_{kin})$ is converted to $P(R_{CC})$ using the reflection principle, i.e., $P(R_{CC}) = P(E_{kin}) \frac{dV_{dicat}}{dR_{CC}}$. The yellow curve in Fig. 2(b) shows that $P(R_{CC})$ peaks at ∼4.6 Å compared to the peak at 3.5 Å of $|\Psi_{v=0}(R_{CC})|^2$ (dashed black curve). These findings stand in stark contrast to the previous works on Ne_2 and Ar_2, dimers where the point charge model was reported to give good agreement between experimental and theoretical interatomic wave functions and equilibrium distances [17,21].

In contrast to, e.g., an Ar^+ ion, a CS_2^+ ion is an extended system and thus an improvement of the point charge model is to place a partial charge on the centers of each of the three atoms. We determined the atomic partial charges from a fit of the electrostatic potential to that calculated from the charge density determined by a DFT method (ωB97X-D) using the diffuse basis set aug-pcseg-1 and the results are given in Fig. 1(b). Now the intermolecular potential of $(CS_2)_2^{2+}$ can be expressed as the sum of the nine pairwise Coulomb interaction terms between the partial charges:

$$V_{partial}(R_{CC}) = \frac{\delta_C^2}{R_{CC}} + 4 \frac{\delta_C \delta_S}{\sqrt{R_{CC}^2 + R_{CS}^2}} + 4 \frac{\delta_S^2}{\sqrt{R_{CC}^2 + 2R_{CS}^2}}, \quad (2)$$

where we assumed that the CS distance, R_{CS}, in each CS_2 monomer remains constant. The $V_{partial}$ potential is depicted in Fig. 3(b).

The red curve in Fig. 2(a) shows $P(E_{kin})$ for the CS_2^+ ions determined from $V_{dicat} = V_{partial}$. The agreement with the measured $P(E_{kin})$ has improved but there is still a 0.3 eV offset between the calculated and the experimental distributions. Using $V_{partial}$ we also converted the measured $P(E_{kin})$ to $P(R_{CC})$, again employing the reflection principle, and as shown in Fig. 2(b) the deviation from $|\Psi_{v=0}(R_{CC})|^2$ is less but remains significant.

Finally, we performed a high-level quantum chemistry calculation of the potential curve, $V_{dicat} = V_{QC}$, for the lowest-energy state, $^3\Sigma$, of $(CS_2)_2^{2+}$. The doubly charged state was calculated with a triplet coupling of the two unpaired electrons with the same level and the same basis sets as the ones used for the ground state of the neutral dimer. Figure 3(b) shows that in the region of the equilibrium distance for $(CS_2)_2$, R_{CC} ∼3.5 Å, V_{QC} lies below both V_{point} and $V_{partial}$. This is due to non-Coulombic effects in the dication. As seen by the blue curve in Fig. 2(a), $P(E_{kin})$ determined from V_{QC} is now very close to the measured distribution with the calculated peak position only ∼26 meV below the experimental position. Correspondingly, $P(R_{CC})$ obtained from conversion of the measured $P(E_{kin})$ via V_{QC} peaks at 3.47 Å, close to the 3.52 Å center of $|\Psi_{v=0}(R_{CC})|^2$, see Fig. 2(b).

IV. DISCUSSION

The non-Coulombic interactions in $(CS_2)_2^{2+}$ can be rationalized as follows. The ionization of each CS_2 monomer removes an electron from the HOMO, a degenerate Π-orbital. Thus, four hole-configurations are possible for the $(CS_2)_2^{2+}$

ion. Using the coordinate system in Fig. 1(a), they are denoted (Π_x^1, Π_y^2), (Π_x^1, Π_z^2), (Π_z^1, Π_y^2), (Π_z^1, Π_z^2), and lead to the formation of four singlet and four triplet states. Spin-orbit interaction between these states lead to 16 energetically different microstates. Our calculations with the hole configurations and the spin-orbit interaction included, show that the 16 microstates energetically fall into three groups as illustrated by the three curves in Fig. 3(c). In the dissociation limit, the first group (four microstates) converges to the $CS_2^+(^2\Pi_{1/2})$–$CS_2^+(^2\Pi_{1/2})$ channel (dotted line), the second group (eight microstates) to the $CS_2^+(^2\Pi_{1/2})$–$CS_2^+(^2\Pi_{3/2})$ channel (dashed line), and the third group (four microstates) to the $CS_2^+(^2\Pi_{3/2})$–$CS_2^+(^2\Pi_{3/2})$ channel (dotted-dashed line). The calculated spin-orbit splitting for the CS_2^+ ion is 47 meV, which can be compared to the experimental value of 55 meV [29].

Our experiment provides neither information about which microstates the laser pulse excites nor information about which fine-structure state ($^2\Pi_{3/2}$ or $^2\Pi_{1/2}$) the CS_2^+ fragment ions end up in. We assume that all 16 microstates are excited with equal probability since the laser-dimer interaction has no specific dependence on these states. If we furthermore assume that the fragmentation occurs adiabatically, i.e., without crossing between the 16 microstates, then E_{kin} of a pair of CS_2^+ fragments is given by the energy difference at $R_{CC} = 3.5$ Å and $R_{CC} \to \infty$ of the curve on which the fragmentation occurred. The resulting E_{kin} distribution obtained from the summation over the 16 fragmentation channels is shown by the black dashed curve in Fig. 2(a). The agreement between the experimental and simulated $P(E_{kin})$ is very good in the region around the peak position. The FWHM of the experimental curve is, however, $\sim$100 meV larger than of the calculated curve, notably towards the low energy side. We believe this asymmetric broadening results from bending excitation of the CS_2^+ ions during the Coulomb fragmentation. For instance, one quantum of bending vibration deposited in each CS_2^+ fragment removes $\sim$85 meV of kinetic energy, which is comparable to the observed broadening.

Our theoretical analysis shows that the experimental $P(E_{kin})$ is the sum of the 16 kinetic energy distributions produced by fragmentation on the potential curves for the 16 microstates. Experimentally, we cannot resolve each of these 16 contributions and therefore, the procedure to convert the experimental $P(E_{kin})$ to $P(R_{CC})$ breaks down. As an approximation we performed the $P(E_{kin}) \to P(R_{CC})$ conversion using the potential curve resulting from an average over the 16 microstates. Such an approximation may provide the correct peak maximum but is likely to overestimate the width. The full black curve in Fig. 2(b) shows that the experimental $P(R_{CC})$ peaks at 3.53 Å, which is only 0.3% larger than the center of the theoretical wave function at 3.52 Å. The experimental $P(R_{CC})$ has a larger width (0.40 Å) compared to the width of the theoretical wave function (0.22 Å) and an asymmetric broadening towards lower R_{CC} values, reflecting the asymmetric broadening of $P(E_{kin})$.

V. CONCLUSION AND PERSPECTIVES

In summary, neither the point-charge nor the partial-charge Coulomb approximation can account for $P(E_{kin})$ of the CS_2^+

recoil ions produced from double ionization of the CS_2 dimer. Similarly, $P(R_{CC})$ obtained from conversion of the measured $P(E_{kin})$ using either the point charge or the partial charge model, deviate strongly from the theoretically calculated intermolecular wave function of the CS_2 dimer. Ab initio calculations showed that the lowest electronic state of $(CS_2)_2^{2+}$ is split into 16 microstates due to different electron (hole) configurations and the spin-orbit coupling. The peak position of $P(E_{kin})$, determined as the average over the 16 microstates, agrees very well with the peak of the experimental $P(E_{kin})$. However, the 16 states implies that, unlike the Coulomb approximation case, there is no longer a unique correspondence between E_{kin} and R_{CC}. Accurate retrieval of the intermolecular wave function from the measured kinetic energy distribution is, therefore, not possible.

The closed-shell electron structure of most molecules and all noble gas atoms, implies that their dimers (or larger complexes) upon multiple ionization, will exhibit a multi microstate structure similar to that of $(CS_2)_2^{2+}$ discussed here (dimers of and complexes with He excluded). At one hand the sensitivity of E_{kin} of the fragment ions from Coulomb explosion to the microstates may provide information about the non-Coulombic interactions in the multiply charged dimer cations. On the other hand, the presence of multiple microstates will in general obstruct accurate conversion of the measured kinetic energy distribution into interatomic/intermolecular distances and wave functions, see Appendix A3.

To substantiate this statement, we calculated the potential curves for the lowest electronic state of the Ar_2^{2+} ion and found that non-Coulombic effects lead to 36 microstates, see Sec. A2. Assuming, as for $(CS_2)_2^{2+}$, that the fragmentation of Ar_2^{2+} occurs adiabatically into the three possible final channels, $Ar^+(^2P_{1/2})$-$Ar^+(^2P_{1/2})$, $Ar^+(^2P_{1/2})$-$Ar^+(^2P_{3/2})$, $Ar^+(^2P_{3/2})$-$Ar^+(^2P_{3/2})$, we find that E_{kin} of the pair of Ar^+ ions lies between 3.52 and 3.64 eV. By comparison, fragmentation via a pure Coulomb curve would give 3.79 eV. Converting a measured $P(E_{kin})$ via the PCA is therefore expected to introduce an error of $\sim$0.2–0.4 Å in the position and width of $P(R)$ compared to $|\Psi_{v=0}(R)|^2$ of Ar_2. Nonadiabatic crossings between the microstates during fragmentation can increase the error further. These considerations have implications for the interpretation of previous works on CEI of weakly bonded dimers [17–21], where the multiply charged molecular cation was modelled by a single Coulomb curve.

The significance of non-Coulombic effects can be minimized by ionizing dimers, or other molecular systems, to higher charge states, ideally empting the valence shell. High intensity fs x-ray pulses from free-electron lasers seem well-suited for this [30–32] and may provide opportunities for Coulomb explosion imaging [32–34].
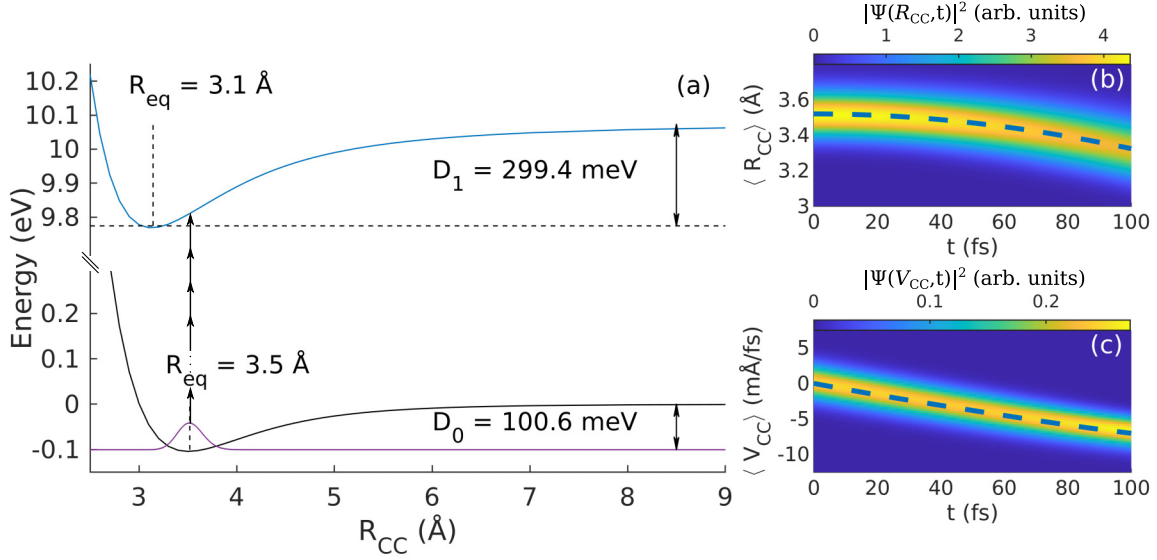
FIG. 4. (a) Potential energy curves for CS_2 (black line) and for $(CS_2)_2^+$ (blue line) potentials. The vibrational ground state of CS_2 (magenta line) is projected by multiphoton absorption onto the $(CS_2)_2^+$ potential. R_{eq} refers to the equilibrium position for each potential and D_0 and D_1 represent the energy difference between the ground vibrational state energy of each potential and its asymptotic energy as $R_{CC} \to \infty$. [(b) and (c)] Time-dependence of $|\Psi(R_{CC}, t)|^2$ and of $|\Psi(V_{CC}, t)|^2$ for the $(CS_2)_2^+$ ion. The mean position of R_{CC} and V_{CC} is represented as a dashed line.

APPENDIX

1. Energy calibration

The Abel inversion to reconstruct the 3D momentum distribution was computed with the polar onion peeling method [35] and then converted to the kinetic energy distribution by a standard Jacobian transformation. To determine the constant of proportionality between the illuminated pixels of the CCD camera and the kinetic energy of the ions, we calibrated the VMI spectrometer using I atoms with a well-defined velocity, obtained by dissociating I_2 molecules through a two-photon transition into either an $I(^2P_{3/2})$-$I(^2P_{3/2})$ pair (I-I) or an $I(^2P_{3/2})$-$I(^2P_{1/2})$ pair (I-I*). The iodine atoms were then ionized 150 ps later by an intense 35-fs, 800-nm laser pulse, and their velocities projected onto the detector. The calibration included measurements at $\lambda = 640$, 660, 680, and 700 nm of the dissociation pulse. The two final states have a dissociation limit energy of $D_0 = 1.543$ eV [36] for (I-I) and $D_1 = 2.485$ eV [36] for (I-I*) and the relative spacing between the two final states therefore gives an energy calibration independent of the wavelength of the dissociation pulse.

2. Intermolecular dynamics of the $(CS_2)_2^+$ dimer

In this section, we calculate if there is any change of R_{CC} after the first ionization and before the second ionization occurs. Any such change of R_{CC} would lead to a blurring or shift of $P(E_{kin})$ of the CS_2^+ ions compared to that expected for directly projecting $|\Psi_{v=0}(R_{CC})|^2$ onto $(CS_2)_2^{2+}$. To describe R_{CC} of the $(CS_2)_2$ dimer after single ionization by the probe pulse, we solve the time-dependent Schrödinger equation on a 1D potential. For this purpose, we use the split-operator method and we apply the kinetic energy operator in the momentum space and the potential energy operator in R_{CC} space

during the propagation of the wave function [37]. The algorithm then solves the equation:

$$\Psi(R_{CC}, t + \Delta t) = \mathcal{F}^{-1} U_{\hat{P}} \mathcal{F} U_{\hat{V}} \mathcal{F}^{-1} U_{\hat{P}} \mathcal{F} \Psi(R_{CC}, t), \quad (A1)$$

$$U_{\hat{P}} = \exp\left(-i \frac{\hat{P}^2}{2\mu} \Delta t / 2\right), \quad (A2)$$

$$U_{\hat{V}} = \exp(-i\hat{V}(R_{CC})\Delta t), \quad (A3)$$

where μ is the reduced mass of $(CS_2)_2$, $\mathcal{F}$ and $\mathcal{F}^{-1}$ stand for the Fourier transform and the inverse Fourier transform operation, $\hat{P}$ and $\hat{V}(R)$ are the momentum and the potential energy operator, respectively, and $\Psi(R_{CC}, t)$ is the intermolecular wave function. We use a grid size for the momentum and the R_{CC} space of 16 384 points to facilitate the Fourier transformation algorithm and a time step of $\Delta t = 1 \times 10^{-17}$ s. The R_{CC} grid starts at 2.4 Å and ends at 9 Å. Fig. 4(a) shows the described process where $\Psi_{v=0}(R_{CC})$ gets projected through multiphoton absorption onto the potential curve of the electronic ground state of $(CS_2)_2^+$. The description of the dynamics is then based on the calculated potential of the first cationic state (with a similar method and basis set as in the main article) following Eq. (A1) and using $\Psi_{v=0}(R_{CC})$ for $(CS_2)_2$ as the initial input. The density of the wave function in R_{CC} and in velocity, V_{CC}, space is shown in Figs. 4(b) and 4(c), respectively. It can be seen that the wave packet moves towards lower value of R_{CC} as expected from the shape of the $(CS_2)_2^+$ potential. The distribution peaks at a negative velocity and gets more confined as a mean velocity is reached for all components of the wave function. This is expected since a Fourier relationship links the R_{CC} and V_{CC} spaces. On each panel, the dashed line shows the mean R_{CC} position and the mean V_{CC} as a function of time. It can be observed that the mean R_{CC} position changes from 3.52 to 3.512 Å

TABLE I. $E_{\rm kin}$ of the Ar^+ fragment ion pairs for the six groups of microstates according to the three possible Ar^+-Ar^+ final channels. The numbers in red are the kinetic energies (expressed in eV) that result from an adiabatic fragmentation.

Final States	Group (degeneracy)					
	1(4)	**2**(8)	**3**(8)	**4**(4)	**5**(8)	**6**(4)
$Ar^+(^2P_{1/2}) + Ar^+(^2P_{1/2})$	3.6409	3.4667	3.4055	3.2955	3.2379	3.1834
$Ar^+(^2P_{1/2}) + Ar^+(^2P_{3/2})$	3.8110	3.6368	3.5756	3.4656	3.4080	3.3535
$Ar^+(^2P_{3/2}) + Ar^+(^2P_{3/2})$	3.9811	3.8069	3.7457	3.6357	3.5781	3.5236

in 20 fs and reaches 3.502 Å in 30 fs. At the 400 nm of the probe pulse, $(CS_2)_2$ is ionized due to absorption of four photons and $(CS_2)_2^+$ due to absorption of five photons. The high non-linearity of these multiphoton processes implies that they both occur close to the peak of the 40 fs long probe pulse, probably within 20 fs of each other. Since our calculation shows that R_{CC} changes to only 3.512 Å from the initial 3.52 Å in 20 fs, we conclude that the motion in the R_{CC} coordinate after single ionization of $(CS_2)_2$ is negligible with our 40 fs probe pulse.

3. Microstates of the argon dimer dication

In double ionization of Ar_2 by the probe pulse, each of the Ar atoms is single ionized by removal of a $3p$ electron. Thus nine hole configurations are possible for the Ar_2^{2+} ion and they can be denoted: (p_x^1, p_x^2), (p_x^1, p_y^2), (p_x^1, p_z^2), (p_y^1, p_x^2), (p_y^1, p_y^2), (p_y^1, p_z^2), (p_z^1, p_x^2), (p_z^1, p_y^2), and (p_z^1, p_z^2). Here the index **1,2** labels the two atoms, and the index x, y, and z the triply degenerate p orbital. The nine hole-configurations lead to the formation of 9 singlet and 9 triplet states for a total of 36 microstates, of which 13 are doubly degenerate. Our calculations, performed at the same computational level as for the $(CS_2)_2^{2+}$ ion, show that the 36 microstates energetically fall into six groups around the Ar_2 equilibrium distance of 3.8 Å, as illustrated by the six curves in Figs. 5(a) and 5(b). In the dissociation limit the six potential curves converge to the final Ar^+-Ar^+ channels:

group 1 (four microstates) $\rightarrow$ $Ar^+(^2P_{1/2})$-$Ar^+(^2P_{1/2})$,
group 2 (eight microstates) $\rightarrow$ $Ar^+(^2P_{1/2})$-$Ar^+(^2P_{3/2})$,
group 3 (eight microstates) $\rightarrow$ $Ar^+(^2P_{1/2})$-$Ar^+(^2P_{3/2})$,
group 4 (four microstates) $\rightarrow$ $Ar^+(^2P_{3/2})$-$Ar^+(^2P_{3/2})$,
group 5 (eight microstates) $\rightarrow$ $Ar^+(^2P_{3/2})$-$Ar^+(^2P_{3/2})$,
group 6 (four microstates) $\rightarrow$ $Ar^+(^2P_{3/2})$-$Ar^+(^2P_{3/2})$.

Table I shows the final $E_{\rm kin}$ of the Ar^+ ion pairs. Similar to the CS_2 dimer case, they are determined by the energy difference at $R = 3.8$ Å and $R \rightarrow \infty$ of the curve on which the fragmentation occurred. The red numbers results from assuming adiabatic fragmentation, i.e., dissociation without any crossing between the 36 microstates, and give rise to $E_{\rm kin}$ between 3.52 and 3.64 eV as stated in the main text. The numbers in black are the kinetic energies that would result from nonadiabatic fragmentation. Clearly such nonadiabaticity in the fragmentation will cause a larger spread of $E_{\rm kin}$ of the Ar^+ fragments.

4. Microstates of dimer dications—general considerations

The microstates arise from the coupling of electronic spin in different orbital occupancy in each of the two ionized frag-

ments and spin-orbit coupling, and the number of microstates thus follows from the electronic spin and the orbital degeneracy of the isolated ionized fragments. If the ionized fragments are nondegenerate, such as Na^+ created from fragmentation of Na_2^{2+} ions, the two singlet states (of Na^+) can only couple to a total singlet state, and thus only one microstate is possible (of Na_2^{2+}). If the ionized fragments are electronic doublet states with doubly degenerate orbitals, such as CS_2^+ created from fragmentation of $(CS_2)_2^{2+}$, the coupling of the two hole configurations leads to four singlet and four triplet states,
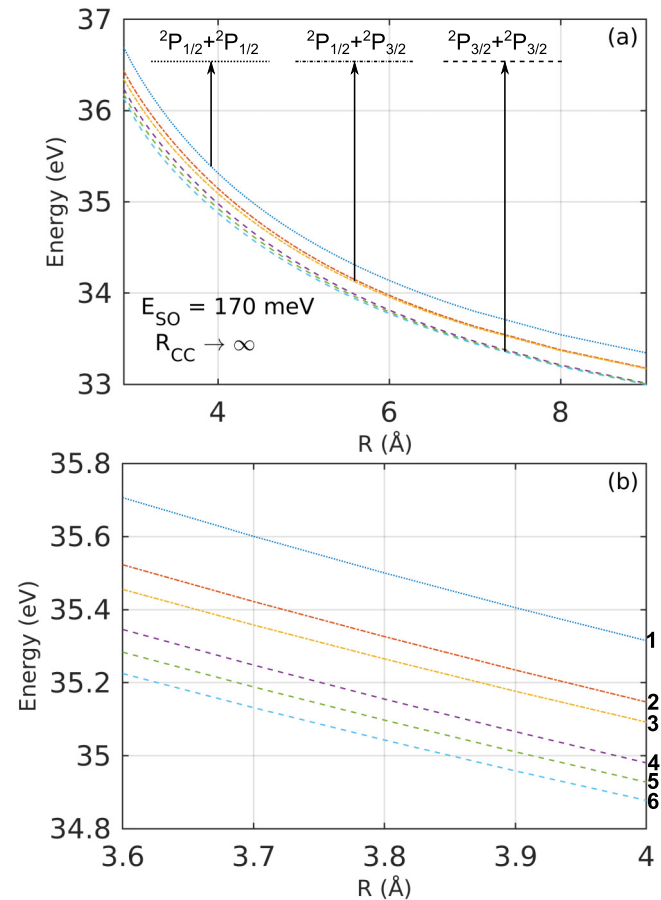
FIG. 5. (a) Potential curves for the six groups of microstates of the lowest electronic state of the Ar_2^{2+}. At $R \rightarrow \infty$, the six groups converge to the three final Ar^+-Ar^+ channels as indicated above. The energy splitting E_{SO} between the curves when $R \rightarrow \infty$ is shown in the legend/on the lower left corner. (b) Close-up of (a) in the region around the equilibrium distance of Ar_2, 3.8 Å. The numbering of the six potential curve is shown on the right y axis of (b). This numbering is used in Table I.

for a total of 16 microstates. In the absence of spin-orbits effect, these 16 microstates have six different energies, while addition of spin-orbit effects leads to 12 different energies. If the ionized fragments are electronic doublet states with triply degenerate orbitals, such as Ar^+ created from fragmentation of Ar_2^{2+}, the coupling of the two hole configurations leads to nine singlet and nine triplet states, for a total of 36 microstates. In the absence of spin-orbit effect, these 36 microstates have 12 different energies, while addition of spin-orbit effects leads to 23 different energies.

These examples cover the most common cases. A more complex system would be $(C_{60})_2^{2+}$ fragmenting into two C_{60}^+ ions, where the electronic doublet states with five times degenerate orbitals would lead to 25 singlet and 25 triplet states, for a total of 100 microstates.

The energy splitting due to different orbital occupancies depends strongly on the inter-fragment distance, while the spin-orbit splitting in addition depends strongly on the atomic number. For Ar_2^{2+} at the van der Waals distance (3.8 Å), the orbital splitting is ∼3000 cm^{-1} (energy difference between lowest and highest state), while the spin-orbit splitting is ∼1300 cm^{-1}, leading to a total splitting of the microstates by ∼4400 cm^{-1}, see Fig. 5(b). For dispersion bound dimers, one expects orbital splitting of the same magnitude as for the Ar dimer, while the orbital splitting will be much larger for systems with a chemical bond. The spin-orbit splitting depends on the atomic number, and Ar_2^{2+} can thus be considered as a system where the two effects are of comparable magnitude. For Ne_2^{2+}, the orbital splitting will dominate, while for the Kr_2^{2+} dication, the spin-orbit splitting will dominate. For most multiply charged dimers (or larger oligomers) of atoms and molecules we, therefore, expect a number of microstates that deviate significantly from the corresponding Coulomb potential. As a result, the conversion of measured kinetic energy distributions of fragments to interatomic/intermolecular distances is obstructed.

[1] Z. Vager, R. Naaman, and E. P. Kanter, Coulomb explosion imaging of small molecules, Science **244**, 426 (1989).

[2] T. Yatsuhashi and N. Nakashima, Multiple ionization and Coulomb explosion of molecules, molecular complexes, clusters and solid surfaces, J. Photochem. Photobiol., C **34**, 52 (2018).

[3] E. P. Kanter, P. J. Cooney, D. S. Gemmell, K. O. Groeneveld, W. J. Pietsch, A. J. Ratkowski, Z. Vager, and B. J. Zabransky, Role of excited electronic states in the interactions of fast (MeV) molecular ions with solids and gases, Phys. Rev. A **20**, 834 (1979).

[4] S. Chelkowski, P. B. Corkum, and A. D. Bandrauk, Femtosecond Coulomb Explosion Imaging of Vibrational Wave Functions, Phys. Rev. Lett. **82**, 3416 (1999).

[5] C. Petersen, E. Péronne, J. Thøgersen, H. Stapelfeldt, and M. Machholm, Control and imaging of interfering wave packets in dissociating I_2 molecules, Phys. Rev. A **70**, 033404 (2004).

[6] F. Légaré, I. V. Litvinyuk, P. W. Dooley, F. Quéré, A. D. Bandrauk, D. M. Villeneuve, and P. B. Corkum, Time-Resolved Double Ionization with Few Cycle Laser Pulses, Phys. Rev. Lett. **91**, 093002 (2003).

[7] T. Ergler, A. Rudenko, B. Feuerstein, K. Zrost, C. D. Schröter, R. Moshammer, and J. Ullrich, Spatiotemporal Imaging of Ultrafast Molecular Motion: Collapse and Revival of the D_2^+ Nuclear Wave Packet, Phys. Rev. Lett. **97**, 193001 (2006).

[8] H. Stapelfeldt, E. Constant, and P. B. Corkum, Wave Packet Structure and Dynamics Measured by Coulomb Explosion, Phys. Rev. Lett. **74**, 3780 (1995).

[9] E. Skovsen, M. Machholm, T. Ejdrup, J. Thøgersen, and H. Stapelfeldt, Imaging and Control of Interfering Wave Packets in a Dissociating Molecule, Phys. Rev. Lett. **89**, 133004 (2002).

[10] C. Cornaggia, D. Normand, and J. Morellec, Role of the molecular electronic configuration in the Coulomb fragmentation of N_2, C_2H_2 and C_2H_4 in an intense laser field, J. Phys. B: At. Mol. Opt. Phys. **25**, L415 (1992).

[11] J. H. Posthumus, A. J. Giles, M. R. Thompson, and K. Codling, Field-ionization, Coulomb explosion of diatomic molecules in intense laser fields, J. Phys. B: At. Mol. Opt. Phys. **29**, 5811 (1996).

[12] D. Mathur, E. Krishnakumar, K. Nagesha, V. R. Marathe, V. Krishnamurthi, F. A. Rajgara, and U. T. Raheja, Dissociation of highly charged CO^{q+} (q ⩾ 2) ions via non-Coulombic potential energy curves, J. Phys. B: At. Mol. Opt. Phys. **26**, L141 (1993).

[13] J. S. Wright, G. A. DiLabio, D. R. Matusek, P. B. Corkum, M. Y. Ivanov, C. Ellert, R. J. Buenker, A. B. Alekseyev, and G. Hirsch, Dissociation of molecular chlorine in a Coulomb explosion: Potential curves, bound states, and deviation from Coulombic behavior for Cl_2^{n+} (n = 2, 3, 4, 6, 8, 10), Phys. Rev. A **59**, 4512 (1999).

[14] C. Wu, Y. Yang, Z. Wu, B. Chen, H. Dong, X. Liu, Y. Deng, H. Liu, Y. Liu, and Q. Gong, Coulomb explosion of nitrogen and oxygen molecules through non-Coulombic states, Phys. Chem. Chem. Phys. **13**, 18398 (2011).

[15] B. Ulrich, A. Vredenborg, A. Malakzadeh, M. Meckel, K. Cole, M. Smolarski, Z. Chang, T. Jahnke, and R. Dörner, Double-ionization mechanisms of the argon dimer in intense laser fields, Phys. Rev. A **82**, 013412 (2010).

[16] B. Manschwetus, H. Rottke, G. Steinmeyer, L. Foucar, A. Czasch, H. Schmidt-Böcking, and W. Sandner, Mechanisms underlying strong-field double ionization of argon dimers, Phys. Rev. A **82**, 013413 (2010).

[17] B. Ulrich, A. Vredenborg, A. Malakzadeh, L. P. H. Schmidt, T. Havermeier, M. Meckel, K. Cole, M. Smolarski, Z. Chang, T. Jahnke, and R. Dörner, Imaging of the structure of the argon and neon dimer, trimer, and tetramer, J. Phys. Chem. A **115**, 6936 (2011).

[18] J. Wu, M. Kunitski, L. P. H. Schmidt, T. Jahnke, and R. Dörner, Structures of N_2Ar, O_2Ar, and O_2Xe dimers studied by Coulomb explosion imaging, J. Chem. Phys. **137**, 104308 (2012).

[19] C. Wu, C. Wu, D. Song, H. Su, X. Xie, M. Li, Y. Deng, Y. Liu, and Q. Gong, Communication: Determining the structure of the N_2Ar van der Waals complex with laser-based channel-selected Coulomb explosion, J. Chem. Phys. **140**, 141101 (2014).

[20] Q. Cheng, X. Xie, Z. Yuan, X. Zhong, Y. Liu, Q. Gong, and C. Wu, Dissociative ionization of argon dimer by intense femtosecond laser pulses, J. Phys. Chem. A **121**, 3891 (2017).

[21] S. Zeller, M. Kunitski, J. Voigtsberger, M. Waitz, F. Trinter, S. Eckart, A. Kalinin, A. Czasch, L. P. H. Schmidt, T. Weber, M. Schoeffler, T. Jahnke, and R. Doerner, Determination of Interatomic Potentials of He₂, Ne₂, Ar₂, and H₂ Wave Function Imaging, Phys. Rev. Lett. **121**, 083002 (2018).

[22] J. Wu, M. Magrakvelidze, A. Vredenborg, L. P. H. Schmidt, T. Jahnke, A. Czasch, R. Dörner, and U. Thumm, Steering the Nuclear Motion in Singly Ionized Argon Dimers with Mutually Detuned Laser Pulses, Phys. Rev. Lett. **110**, 033005 (2013).

[23] B. Shepperson, A. S. Chatterley, A. A. Søndergaard, L. Christiansen, M. Lemeshko, and H. Stapelfeldt, Strongly aligned molecules inside helium droplets in the near-adiabatic regime, J. Chem. Phys. **147**, 013946 (2017).

[24] A. S. Chatterley, M. O. Baatrup, C. A. Schouder, and H. Stapelfeldt, Laser-induced alignment dynamics of gas phase CS₂ dimers, Phys. Chem. Chem. Phys. **22**, 3245 (2020).

[25] J. H. Posthumus, The dynamics of small molecules in intense laser fields, Rep. Prog. Phys. **67**, 623 (2004).

[26] M. Rezaei, J. Norooz Oliaee, N. Moazzen-Ahmadi, and A. R. W. McKellar, Spectroscopic observation and structure of CS₂ dimer, J. Chem. Phys. **134**, 144306 (2011).

[27] F. B. van Duijneveldt, J. G. C. M. van Duijneveldt-van de Rijdt, and J. H. van Lenthe, State of the art in counterpoise theory, Chem. Rev. **94**, 1873 (1994).

[28] T. Helgaker, W. Klopper, H. Koch, and J. Noga, Basis-set convergence of correlated calculations on water, J. Chem. Phys. **106**, 9639 (1997).

[29] S.-G. He and D. J. Clouthier, The molecular structure and a Renner-Teller analysis of the ground and first excited electronic states of the jet-cooled CS₂⁺ molecular ion, J. Chem. Phys. **124**, 084312 (2006).

[30] L. Young, E. P. Kanter, B. Krässig, Y. Li, A. M. March, S. T. Pratt, R. Santra, S. H. Southworth, N. Rohringer, L. F. DiMauro, G. Doumy, C. A. Roedig, N. Berrah, L. Fang, M. Hoener, P. H. Bucksbaum, J. P. Cryan, S. Ghimire, J. M. Glownia, D. A. Reis, J. D. Bozek, C. Bostedt, and M. Messerschmidt, Femtosecond electronic response of atoms to ultra-intense X-rays, Nature **466**, 56 (2010).

[31] G. Doumy, C. Roedig, S.-K. Son, C. I. Blaga, A. D. DiChiara, R. Santra, N. Berrah, C. Bostedt, J. D. Bozek, P. H. Bucksbaum,

J. P. Cryan, L. Fang, S. Ghimire, J. M. Glownia, M. Hoener, E. P. Kanter, B. Krässig, M. Kuebel, M. Messerschmidt, G. G. Paulus, D. A. Reis, N. Rohringer, L. Young, P. Agostini, and L. F. DiMauro, Nonlinear Atomic Response to Intense Ultrashort X Rays, Phys. Rev. Lett. **106**, 083002 (2011).

[32] A. Rudenko, L. Inhester, K. Hanasaki, X. Li, S. J. Robatjazi, B. Erk, R. Boll, K. Toyota, Y. Hao, O. Vendrell, C. Bomme, E. Savelyev, B. Rudek, L. Foucar, S. H. Southworth, C. S. Lehmann, B. Kraessig, T. Marchenko, M. Simon, K. Ueda, K. R. Ferguson, M. Bucher, T. Gorkhover, S. Carron, R. Alonso-Mori, J. E. Koglin, J. Correa, G. J. Williams, S. Boutet, L. Young, C. Bostedt, S.-K. Son, R. Santra, and D. Rolles, Femtosecond response of polyatomic molecules to ultra-intense hard X-rays, Nature (London) **546**, 129 (2017).

[33] S. Zeller, M. Kunitski, J. Voigtsberger, A. Kalinin, A. Schottelius, C. Schober, M. Waitz, H. Sann, A. Hartung, T. Bauer, M. Pitzer, F. Trinter, C. Goihl, C. Janke, M. Richter, G. Kastirke, M. Weller, A. Czasch, M. Kitzler, M. Braune, R. E. Grisenti, W. Schöllkopf, L. P. H. Schmidt, M. S. Schöffler, J. B. Williams, T. Jahnke, and R. Dörner, Imaging the He₂ quantum halo state using a free electron laser, Proc. Natl. Acad. Sci. USA **113**, 14651 (2016).

[34] T. Takanashi, K. Nakamura, E. Kukk, K. Motomura, H. Fukuzawa, K. Nagaya, S.-i. Wada, Y. Kumagai, D. Iablonskyi, Y. Ito, Y. Sakakibara, D. You, T. Nishiyama, K. Asa, Y. Sato, T. Umemoto, K. Kariyazono, K. Ochiai, M. Kanno, K. Yamazaki, K. Kooser, C. Nicolas, C. Miron, T. Asavei, L. Neagu, M. Schöffler, G. Kastirke, X.-J. Liu, A. Rudenko, S. Owada, T. Katayama, T. Togashi, K. Tono, M. Yabashi, H. Kono, and K. Ueda, Ultrafast Coulomb explosion of a diiodomethane molecule induced by an X-ray free-electron laser pulse, Phys. Chem. Chem. Phys. **19**, 19707 (2017).

[35] K. Zhao, T. Colvin, W. T. Hill, and G. Zhang, Deconvolving two-dimensional images of three-dimensional momentum trajectories, Rev. Sci. Instrum. **73**, 3044 (2002).

[36] R. J. LeRoy, Spectroscopic reassignment and ground-state dissociation energy of molecular iodine, J. Chem. Phys. **52**, 2678 (1970).

[37] M. D. Feit, J. A. Fleck Jr., and A. Steiger, Solution of the Schrödinger equation by a spectral method, J. Comp. Phys. **47**, 412 (1982).

[38] J. D. Pickering, B. Shepperson, B. A. Hübschmann, F. Thorning, and H. Stapelfeldt, Alignment and Imaging of the CS₂ Dimer Inside Helium Nanodroplets, Phys. Rev. Lett. **120**, 113202 (2018).